Anisotropic nanoparticles immersed in a nematic liquid crystal: Defect structures and potentials of mean force

Francisco R. Hung,[1] Orlando Guzmán,[1,2] Brian T. Gettelfinger,[1] Nicholas L. Abbott,[1] and Juan J. de Pablo[1,*]
[1]*Department of Chemical and Biological Engineering, University of Wisconsin, Madison, Wisconsin 53706-1691, USA*
[2]*Departamento de Física, Universidad Autónoma Metropolitana-Iztapalapa, México D. F., Mexico*
(Received 13 March 2006; revised manuscript received 26 May 2006; published 27 July 2006)

We report results for the potential of mean force (PMF) and the defect structures that arise when spherocylindrical nanoparticles are immersed in a nematic liquid crystal. Using a dynamic field theory for the tensor order parameter **Q** of the liquid crystal, we analyzed configurations, including one, two, and three elongated particles, with strong homeotropic anchoring at their surfaces. For systems with one nanoparticle, the most stable configuration is achieved when the spherocylinder is placed with its long axis perpendicular to the far-field director, for which the defect structure consists of an elongated Saturn ring. For systems with two or three nanoparticles with their long axes placed perpendicular to the far-field director, at small separations the defect structures consist of incomplete Saturn rings fused with new disclination rings orthogonal to the original ones, in analogy to results previously observed for spherical nanoparticles. The shape of these orthogonal rings depends on the nanoparticles' configuration, i.e., triangular, linear, or parallel with respect to their long axis. A comparison of the PMFs indicates that the latter configuration is the most stable. The stability of the different arrays depends on whether orthogonal disclination rings form or not, their size, and the curvature effects in the interparticle regions. Our results suggest that the one-elastic-constant approximation is valid for the considered systems; similar results were obtained when a three-constant expression is used to represent the elastic free energy. The attractive interactions between the elongated particles were compared to those observed for spheres of similar diameters. Similar interparticle energies were observed for linear arrays; in contrast, parallel and triangular arrays of spherocylinders yielded interactions that were up to 3.4 times stronger than those observed for spherical particles.

DOI: 10.1103/PhysRevE.74.011711 PACS number(s): 61.30.Jf, 77.84.Nh, 61.30.Cz, 42.79.Kr

I. INTRODUCTION

Liquid crystals are finding emerging applications in a wide variety of fields. One example is the use of liquid crystals in chemical and biomolecular sensors [1–3]. The sensing mechanism is remarkably simple; the presence of chemicals or biomolecules perturbs the local ordering of a liquid crystal, and triggers the formation of inhomogeneous textures. Due to the long-range order of the liquid crystals, these inhomogeneities can be communicated over several length scales, e.g., from a nanometer-sized protein to the size of a disclination line, on the order of tenths of millimeters. Therefore, the optical signatures can be detected by simply using a microscope and polarized light [1–3]. A second example is provided by the use of liquid crystals as tunable solvents for microemulsions and particle dispersions [4–8]; in such systems, the elastic distortion of the liquid crystal induced by the presence of the particles can give rise to long-range interparticle interactions, which are absent when colloids or droplets are dispersed in isotropic solvents. Particle or droplet suspensions in liquid crystals have potential applications for development of new composite materials with improved physical properties [4–8].

The main objects responsible for the response of a biosensor or the structure of a microemulsion or suspension are the defects that arise around a specific nanoparticle or a collection of nanoparticles. Optimization of the applications mentioned above therefore requires a fundamental understanding of the structure and dynamics of topological defects around particles immersed in a liquid crystal, as well as the liquid crystal-induced interparticle interactions that arise due to elastic distortions. The uniform alignment of a nematic is usually distorted by the particles, due to the constraints imposed by the anchoring of the liquid crystal at their surfaces. Topological defects are observed when these constraints impose conflicting orientations to the liquid crystal, giving rise to discontinuities in the director field $\mathbf{n}(\mathbf{r})$ [9]. The defect core itself is characterized by strong biaxiality and a pronounced decrease in the scalar order parameter $S(\mathbf{r})$, which measures the degree of orientational order; a low value of $S(\mathbf{r})$ reflects the fact that the liquid crystal "melts" locally at the defect core [9,10]. Experimentally, three types of defects have been observed when a spherical particle is placed in a nematic liquid crystal: the dipole configuration or hyperbolic hedgehog [4,11], the quadrupolar configuration or Saturn ring [12,13], and the surface-ring configuration or boojum [11]. They have been the subjects of a number of theoretical and numerical studies [14–18]. In particular, Stark [17,18] used a director description of the liquid crystal to show that the hedgehog configuration is stable for strong surface anchoring and μm-sized spherical particles. The Saturn ring configuration becomes stable when the particle size is reduced or when a magnetic field is applied; confining the particle is also predicted to stabilize a Saturn ring configuration [19]. A surface ring defect is observed upon reduction of the surface anchoring strength [17,18]. Recent calculations using a tensor order parameter description of the liquid crys-

*Electronic address: depablo@engr.wisc.edu

tal and an adaptive mesh refinement scheme confirmed these conclusions [20]. This methodology was extended very recently to study a system of two μm-sized spheres in a nematic liquid crystal, where each particle exhibits a hyperbolic hedgehog defect [21,22]. A similar system, consisting of a pair of nanoscopic spherical particles surrounded by Saturn ring defects, was studied recently using both Monte Carlo molecular simulations and a continuum field theory for the liquid crystal tensor order parameter **Q** [23,24]; in both approaches, a third disclination ring orthogonal to the original ones was observed between the two spheres at short separations. Given the good agreement between molecular simulations and the field theory, the latter approach was extended to study a system of three spherical nanoparticles immersed in a nematic liquid crystal [25], and also to study the structure and dynamics of a nematic in a two-dimensional (2D) representation of a liquid crystal sensor [1,2], where chemicals or biomolecules (represented as spherical nanoparticles) can adsorb at the sensor walls [26,27].

Several simulation and numerical studies have considered the case of elongated particles immersed in a liquid crystal. In addition to their relevance for liquid crystal sensors and particle dispersions, anisotropic particles have been considered in recent experiments by Lapointe and co-workers, who showed that for a system of nanowires placed in a nematic, controlled variations in the liquid crystal director field could levitate the nanowires to a specified height [28,29]. Burylov and Raikher [30] used a continuum theory in terms of the liquid crystal director **n** to study the equilibrium orientation of an elongated particle immersed in a nematic. Andrienko *et al.* [31] used molecular dynamics and Monte Carlo simulations to examine the defect structures and torque around an spherocylindrical particle and a rod of infinite length placed in a nematic. In later studies, Andrienko and co-workers also used a Landau–de Gennes free energy in terms of the liquid crystal tensor order parameter **Q** to determine the interactions between pairs of infinitely long cylindrical particles immersed in a nematic [32], and in a nematic-isotropic interface [33,34]. Similarly, McKay and Virga [35] used a free energy in terms of **Q** to study the force and torque exerted on an infinitely long cylinder placed in a nematic when the cylinder is close to a wall. Most of these studies have considered elongated particles of infinite length, which were often modeled as disks in a 2D system. Only one of these previous studies [31] has considered the case of a single anisotropic particle of finite length. Results for two spheres have been reported in several studies ([21–24] and references therein), and systems of more particles have been considered in just a few investigations [25,36,37]; interestingly, Yamamoto *et al.* [36,37] have considered a 2D system where the disks are free to move due to the many-body forces mediated by nematic and smectic-C* solvents.

In this paper, we report numerical calculations for the defect structures that arise when spherocylindrical nanoparticles are immersed in a 3D nematic liquid crystal. A Landau–de Gennes free energy in terms of the tensor order parameter **Q** is used to represent the nematic solvent. Different configurations with one, two, and three elongated nanoparticles with strong homeotropic anchoring are considered. We also calculate the potential of mean force (PMF) for the different systems. The PMF gives the difference in free energy between two states, as a function of a specific degree of freedom of the system, namely the orientation angle θ for one-particle systems, and the minimum surface-to-surface interparticle distance d for the case of two- and three-particle systems. The paper is organized as follows. In Sec. II we present a description of our model systems and details of the numerical methodology. Our results are presented and discussed in Sec. III. Section IV includes some concluding remarks and suggestions for future work.

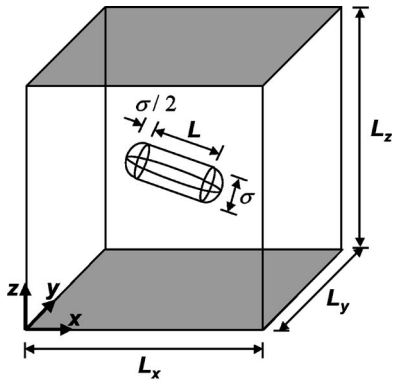

FIG. 1. Scheme of the model system for one anisotropic nanoparticle.

II. MODELS AND METHODS

A. Details of the model systems

The model system considered in this work consists of a rectangular box of dimensions L_x, L_y, and L_z, containing one, two, or three elongated nanoparticles immersed in a nematic liquid crystal. A schematic representation of the model system for one particle is shown in Fig. 1. The nanoparticles are represented by a cylinder of length $L=24.8$ nm and spherical caps of diameter $\sigma=12.4$ nm, so that the total length of the spherocylinder is 37.2 nm. These dimensions are comparable to the particle size considered in the molecular simulations of Andrienko and co-workers [31], and a direct comparison between their results and ours is therefore possible. As in our previous studies [23–25], periodic boundary conditions are imposed in the x and y directions. The top and bottom of the simulation box consist of walls that impose strong homeotropic anchoring to the liquid crystal. In the absence of particles, the system exhibits a homogeneous texture where the director field $\mathbf{n}(\mathbf{r})$ is parallel to the z axis. Homeotropic anchoring of the liquid crystal is also imposed at the nanoparticle surfaces. For brevity, when we refer to the "placement" and "orientation" of an spherocylindrical particle in this paper, we mean the placement of its center of mass and the orientation of its long axis, respectively. In addition, when we refer to the "separation" between particles, we denote the minimum surface-to-surface distance between spherocylinders.

In all cases considered in this work, the particles lie in a common plane that passes through the center of the simulation box. For one-particle systems, we considered different

configurations where the spherocylinder is oriented at an angle θ with respect to the x axis in the x-z plane (see Fig. 2). For two-particle systems, three arrays were considered where the particles are oriented along the x axis, but the particles are placed in different ways (see Fig. 5): (a) centers are on the x axis (linear array); (b) centers are on the y axis (parallel x-y array); and (c) centers are on the z axis (parallel x-z array). The same arrays were considered for three-particle systems, together with an additional arrangement (d) where the particles' long axes lie at the sides of an equilateral triangle in the x-y plane (triangular array, see Fig. 10). The PMF and the defect structures were determined as a function of the angle θ for one-particle systems, and as a function of the particle separation d for the case of two- and three-particle systems. Different simulation box sizes were considered, depending on the number of particles. A cubic simulation box with $L_x=L_y=L_z=114$ nm was used for one-particle systems. For the systems with two and three nanoparticles, the dimensions of the simulation box were $L_x=L_y=202$ nm, $L_z=80$ nm for all cases except the parallel x-z arrays, where a box with $L_x=L_z=202$ nm and $L_y=80$ nm was used.

B. Dynamic field theory for the nematic liquid crystal

The behavior of the nematic was modeled using a dynamic field theory for the tensor order parameter $\mathbf{Q}(\mathbf{r})$; in contrast to the director field $\mathbf{n}(\mathbf{r})$, $\mathbf{Q}(\mathbf{r})$ is free of divergences and discontinuities even at the disclination lines. The local values of the scalar order parameter $S(\mathbf{r})$ and the director $\mathbf{n}(\mathbf{r})$ can be obtained from $\mathbf{Q}$ through its largest eigenvalue $2S/3$ and its associated eigenvector, respectively [9]. In previous studies [23,24], it was shown that results obtained from this theory are in agreement with those from molecular simulations, down to length scales comparable to the size of a liquid crystal molecule. This theory corresponds to a particular case of the Beris-Edwards formulation of the thermodynamics of fluids with internal microstructure [38]. In this formulation, the evolution of the tensor order parameter $\mathbf{Q}$ as a function of position $\mathbf{r}$ and time t is determined by the functional derivative of the system free energy F with respect to $\mathbf{Q}$,

$$\frac{\partial \mathbf{Q}}{\partial t} = -\frac{1}{\gamma}\left[\frac{\delta F}{\delta \mathbf{Q}} - \frac{1}{3}\mathrm{Tr}\left(\frac{\delta F}{\delta \mathbf{Q}}\right)\mathbf{I}\right]. \tag{1}$$

Here γ is a kinetic coefficient associated with the rotational viscosity of the liquid crystal, and for simplicity it is assumed to be a constant. In this equation, it is assumed that $\delta F/\delta \mathbf{Q}$ has been symmetrized. The free energy F of the liquid crystal includes three contributions,

$$F = \int d\mathbf{r}\, f_{LdG}(\mathbf{r}) + \int d\mathbf{r}\, f_e(\mathbf{r}) + \oint dS f_s(\mathbf{r}). \tag{2}$$

The first term, f_{LdG}, represents a Landau–de Gennes expansion describing the short-range interactions that drive the bulk isotropic-nematic phase transition

$$f_{LdG} = \frac{A}{2}\left(1-\frac{U}{3}\right)\mathrm{Tr}(\mathbf{Q}^2) - \frac{AU}{3}\mathrm{Tr}(\mathbf{Q}^3) + \frac{AU}{4}[\mathrm{Tr}(\mathbf{Q}^2)]^2. \tag{3}$$

The phenomenological coefficients A and U depend on the liquid crystal of interest. A controls the energy scale of the model, whereas U controls the value of the bulk scalar order parameter S,

$$S_{bulk} = \frac{1}{4}\left(1+3\sqrt{1-\frac{8}{3U}}\right). \tag{4}$$

In this model, the system is isotropic for $0<U<2.7$, and nematic for $U>2.7$. The limits of metastability for the isotropic and nematic phases are $U=3$ and $8/3$, respectively. The third term in Eq. (2) represents the surface contribution to the free energy, and accounts for the liquid crystal anchoring at the surfaces. We only consider the case of strong homeotropic anchoring at all surfaces. In this limit case, the prescribed perpendicular orientation of the liquid crystal at every surface must be satisfied, lest f_s diverges. In our calculations, the homeotropic anchoring of the liquid crystal at every surface is enforced through the boundary conditions.

The second term in Eq. (2) describes the long-range elastic forces of the liquid crystal, and introduces a free energy penalty associated with gradients of the tensor order parameter field. Two expressions have been used to evaluate the elastic free energy of the liquid crystal: the one-elastic-constant approximation, and a three-elastic-constant expression proposed by Edwards *et al.* [38–40]. We explain those in detail in the following sections.

1. One-elastic-constant approximation

For simplicity, we have used in most of our calculations the one-elastic-constant approximation [9], where the splay, twist, and bend elastic constants K_{11}, K_{22}, and K_{33} have a common value. The elastic free energy takes the following form:

$$f_e = \frac{L_1}{2}\partial_k Q_{ij}\partial_k Q_{ij}. \tag{5}$$

In Eq. (5), $i,j,k \in x,y,z$, and the Einstein summation convention over repeated indexes is used (this convention is also assumed in subsequent equations). When the functional derivatives in Eq. (1) are evaluated with Eq. (5) for the elastic free energy, the following partial differential equation for $\mathbf{Q}$ is obtained:

$$\frac{\partial Q_{ij}}{\partial t} = -\frac{1}{\gamma}\left\{A\left(1-\frac{U}{3}\right)Q_{ij} - AU\left[Q_{ik}Q_{kj} - \frac{\delta_{ij}}{3}Q_{kl}Q_{kl} - Q_{ij}(Q_{kl}Q_{kl})\right] - L_1\partial_k\partial_k Q_{ij}\right\}, \tag{6}$$

where the indexes $i,j,k,l \in x,y,z$. Equation (6) was solved numerically for all systems considered in this study. The values of the dimensionless parameters are $A=1$, $U=6$, $\gamma=400$, and $L_1=1$, corresponding to $S_{bulk}=0.81$. Given suitable scaling factors for pressure (10^5 Pa), length (10 nm),

and time (1 ns), these parameters correspond to a material having an elastic constant $K=5$ pN (within the one-elastic-constant approximation), and an orientational viscosity $\gamma=0.04$ Pa s. These values are representative of a low molecular-weight liquid crystal, such as 5*CB*. In addition, from a dimensional analysis one can obtain a characteristic length scale for the spatial variations of **Q** [10], $\xi=\sqrt{18L_1/AU}$, which corresponds to $\xi=17.3$ nm for our parameters.

2. Three-elastic-constant expression of Edwards et al. [38–40]

One of the issues of the one-elastic-constant approximation is that it cannot distinguish bend from splay elastic constants (i.e., $K_{11}=K_{33}$). Complete expressions have been derived for the elastic free energy (see, e.g., Refs. [41,42]). For example, the theoretical form proposed by Longa *et al.* [41] involves a fourth-order expression in terms of **Q** and its gradient, and nineteen elastic coefficients are required. Note, however, that several theoretical studies [38–40,42,43] have demonstrated that to remove the restriction $K_{11}=K_{33}$, it is enough to include higher moments in the orientation distribution function, or to simply incorporate higher order terms in **Q** in the elastic free energy. One simple extension has been proposed by Edwards *et al.* [38–40], and involves a cubic term in **Q** and its gradient. This expression for the elastic free energy includes three different values for the splay, twist, and bend elastic constants (K_{11}, K_{22}, and K_{33}). In contrast to the expression of Longa *et al.*, which requires nineteen elastic coefficients [41], the expression of Edwards *et al.* requires just three parameters (L_1, L_2, and L_3), and was therefore adopted for some of our calculations,

$$f_e=\frac{L_1}{2}\partial_k Q_{ij}\partial_k Q_{ij}+\frac{L_2}{2}\partial_i Q_{ik}\partial_j Q_{jk}+\frac{L_3}{2}Q_{ij}\partial_i Q_{kl}\partial_j Q_{kl}. \quad (7)$$

The coefficients L_1, L_2, and L_3 are related to the splay, twist, and bend constants K_{11}, K_{22}, and K_{33} as follows:

$$L_1=\frac{3K_{22}-K_{11}+K_{33}}{6S^2}, \quad (8)$$

$$L_2=\frac{K_{11}-K_{22}}{S^2}, \quad (9)$$

$$L_3=\frac{K_{33}-K_{11}}{2S^3}. \quad (10)$$

When the functional derivatives from Eq. (1) are evaluated with Eq. (7) for the elastic free energy, the following partial differential equation is obtained [40]:

$$\frac{\partial Q_{ij}}{\partial t}=-\frac{1}{\gamma}\left\{A\left(1-\frac{U}{3}\right)Q_{ij}-AU\left[Q_{ik}Q_{kj}-\frac{\delta_{ij}}{3}Q_{kl}Q_{kl}-Q_{ij}(Q_{kl}Q_{kl})\right]-L_1\partial_k\partial_k Q_{ij}-L_2\left[\frac{1}{2}\partial_k\partial_i Q_{kj}+\frac{1}{2}\partial_k\partial_j Q_{ki}-\frac{\delta_{ij}}{3}\partial_k\partial_l Q_{kl}\right]+L_3\left[\frac{1}{2}\partial_i Q_{kl}\partial_j Q_{kl}-Q_{kl}\partial_l\partial_k Q_{ij}-\partial_k Q_{kl}\partial_l Q_{ij}-\frac{\delta_{ij}}{6}\partial_m Q_{kl}\partial_m Q_{kl}\right]\right\}, \quad (11)$$

where the indexes $i,j,k,l\in x,y,z$, and Einstein's summation convention is used. The dimensionless parameters in Eq. (11) have values $A=1$, $U=6$, and $\gamma=400$, which correspond to $S_{bulk}=0.81$, and were obtained following the same procedure described in the previous section. We have calculated $L_1=0.733$, $L_2=0.800$, and $L_3=0.800$, from Eqs. (8)–(10) and experimental values recently reported for 5*CB* [44] for the elastic constants ($K_{11}=5$ pN, $K_{22}=3$ pN, and $K_{33}=7$ pN). Equation (11) was solved numerically just for the two-particle configurations, in order to determine the possible effect of splay and bend distortions in our systems.

C. Simulation details

Equations (6) and (11) were solved for the five independent components of **Q** (Q_{xx}, Q_{yy}, Q_{xy}, Q_{xz}, and Q_{yz}, since **Q** is traceless) using the finite element computational package COMSOL Multiphysics™ [45]. In order to solve the equations, we used the time-dependent algorithm DASPK, combined with the linear system solver GMRES and the incomplete LU preconditioner [45]. Equation (6) was solved for a sufficiently long time to observe negligible variations in the numerical solution with respect to time, which corresponds to finding the solution that minimizes the free energy [the right-hand side of Eq. (6) and (11)]. We performed three-dimensional simulations using unstructured meshes containing tetrahedral, linear Lagrange elements [46]. Different grid densities were used, and it was found that for the solutions to be independent of further mesh refinements, 20 240, 24 810, and 32 060 finite elements were required in systems with one, two, and three particles. The mesh was significantly finer in the immediate vicinity of the nanoparticles, where strong variations in **Q** are expected. In addition, much smaller elements were required close to the nanoparticles' spherical tips, due to important curvature effects. The minimum length size of the finite elements was approximately 2.6×10^{-3} nm for systems containing one nanoparticle, and 1.1×10^{-3} nm for systems with two and three spherocylinders. These finest grid sizes correspond to $2.1\times10^{-4}\sigma$ and $8.9\times10^{-5}\sigma$ (where σ is the spherocylinder diameter), and are comparable to those reported by Fukuda *et al.* [20] in their adaptive mesh refinement scheme. The initial conditions of **Q** in our simulations are such that the director **n** is initially aligned along the z direction, and the scalar order parameter S was initially fixed to the equilibrium value $S_{bulk}=0.81$ [Eq. (4)]. For completeness, several runs were also started from conditions giving an initial random configuration of the director field; it was found that the final numerical solutions were independent of the initial conditions. The scalar order parameter at the nanoparticles' surface was also set to $S=S_{bulk}=0.81$. Different methods are available to visualize the defect structures (see, e.g., Refs. [47–49]). In this work, we follow literature studies [23–25] and choose the contour $S=0.25$ to visualize the defects that arise for specific numerical solutions, since it corresponds to the smallest value of S for a stable bulk nematic in our par-

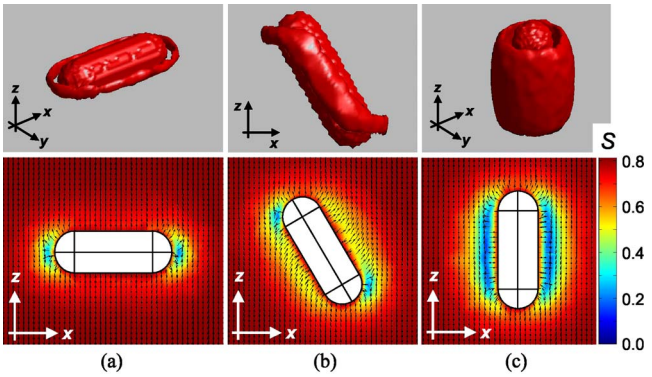

FIG. 2. (Color online) 3D visualizations of the defect structures (represented as the contour $S=0.25$, top), and contour maps of the scalar order parameter S superimposed with the director field in the x-z plane (bottom), for (a) $\theta=0°$, (b) $\theta=60°$, and (c) $\theta=90°$.

ticular model [10,38]. The free energy values used in the computation of the potential of mean force were determined by numerical integration of Eqs. (2), (3), and (5) (for the one-elastic-constant approximation) or Eq. (7) (when using the three-elastic-constant expression of Edwards *et al.* [38–40]) over the volume of the system.

III. RESULTS AND DISCUSSION

A. One-particle systems

As mentioned before, one of our aims is to determine the defect structures and the potential of mean force that arise when spherocylindrical nanoparticles are immersed in a nematic liquid crystal. First, we consider the situation where a single anisotropic nanoparticle lies in the x-z plane, oriented with its long axis at an angle θ with respect to the x axis. The director **n** is parallel to the z axis far away from the particle, which exhibit homeotropic anchoring at its surface, and the one-elastic-constant approximation was used. In Fig. 2 we present contour maps of the scalar order parameter S in the x-z plane, for $\theta=0°$, 60°, and 90°. The corresponding director fields are superimposed to those maps. The defect structures are visualized as the surface $S=0.25$. For $\theta=0°$, the defect structure is a Saturn ring elongated in the direction of the spherocylinder long axis [Fig. 2(a)]. Such a defect structure was expected to be the stable one for particles with nanoscopic size [17,18]. As the angle θ increases, the Saturn ring "bends:" close to the spherical caps, the disclination line remains in a horizontal position, whereas close to the cylindrical body it runs parallel to the long axis of the nanoparticle [Fig. 2(b)]. Moreover, close to the cylinder the defect core widens gradually as θ increases, until it eventually surrounds the cylindrical section of the particle and forms the defect structure observed for $\theta=90°$ [Fig. 2(c)]. These results are in good agreement with those reported by Andrienko and co-workers [31], who studied a similar system using molecular dynamics and Monte Carlo simulations. However, when the spherocylinder is parallel to the far-field director ($\theta=90°$), Andrienko *et al.* reported that the director distribution around the particle is not axially symmetric, causing a nonzero torque; they did not observe a configuration with axial symmetry, even though it is physically possible [31]. In contrast, the dynamic field theory predicts an axially symmetric solution for this case. Andrienko *et al.* [31] did not report the values of the elastic constants for their system, and so it is not possible to perform a detailed comparison. In addition, the theory does not take into account effects due to liquid crystal density inhomogeneities and packing around the elongated nanoparticles, which may be responsible for the discrepancies observed between our results and those from Ref. [31] for $\theta=90°$. A previous study [24] has considered the case of two spheres immersed in a liquid crystal using both dynamical field theory and molecular simulations. Good agreement between both approaches was found down to length scales comparable to the mesogens size, but for smaller interparticle separations it was concluded that the effect of density inhomogeneities in the liquid crystal needed to be included in the theory in order to obtain defect structures similar to those observed from molecular simulations. Aside from the particular case of an spherocylinder with $\theta=90°$, the agreement between dynamic field-theoretic results and the molecular simulations of Andrienko and co-workers [31] is excellent.

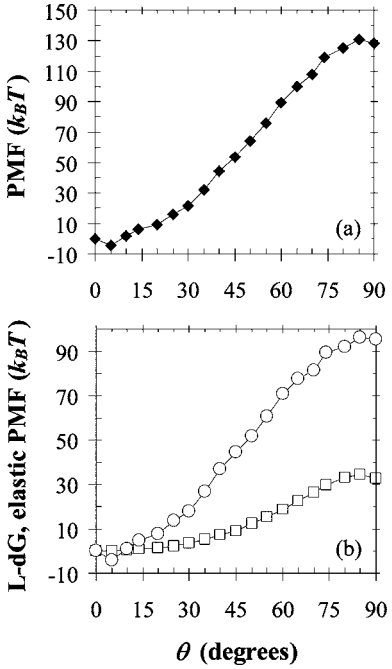

FIG. 3. Potential of mean force (PMF) for one nanoparticle immersed in a nematic liquid crystal, as a function of the angle θ with respect to the x axis. (a) Total PMF; (b) Landau–de Gennes (LdG, squares), and elastic (circles) contributions to the PMF.

Figure 3(a) depicts the free energy of the system as a function of the orientation θ. For each angle, the free energy was calculated as the difference of free energy F with respect to that for the case of $\theta=0°$. The lowest free energy values are observed for configurations where the nanoparticle is perpendicular to the director field, i.e., $\theta\sim 0°-10°$ (the difference in free energy among these configurations is on the order of a few k_BT). In Fig. 3(b) we show plots of the Landau–de Gennes (LdG) and elastic contributions to the

free energy [Eq. (2)]. Both curves exhibit the same behavior as the total free energy curve (i.e., minima at $\theta \sim 0° - 10°$, maxima at $\theta \sim 85° - 90°$), but the difference between maxima and minima is larger for the elastic contribution ($\sim 100 k_B T$, against $\sim 30 k_B T$ for the LdG term). These results suggest that elastic effects are more important, and configurations with smaller gradients in the director field will be preferred. The Saturn ring defect structures obtained for low θ values exhibit smaller surface areas than those observed for higher θ values (see Fig. 2). The elastic free energy penalties are therefore smaller for configurations with low θ, and as a result, these are significantly more stable than their high-θ counterparts. The free energy differences among these can reach values as large as 130 $k_B T$ (Fig. 3).

B. Two-particle systems

1. One-elastic-constant approximation

In view of the results for uniparticle systems, and given the computational demands of the calculations presented in this work, our analysis of two- and three-particle systems is limited to configurations where the spherocylinders are perpendicular to the far-field director. As mentioned in Sec. II, for two-particle systems we considered three cases: (a) a linear array, (b) a parallel array in the x-y plane, and (c) a parallel array in the x-z plane. In all cases the director field **n** is parallel to the z axis far away from the spherocylinders, as it was previously considered for the one-particle systems, and the one-elastic-constant approximation was used.

The potential of mean force (PMF) was determined as a function of the minimum surface-to-surface interparticle distance d; these results are presented in Fig. 4. In this case, the PMF represents the free energy difference of a given two-particle configuration, with respect to a situation where they are infinitely apart. The total PMF [Fig. 4(a)] for all arrays becomes negative as the separation d is reduced. The PMF for the parallel x-y array becomes negative at the largest separation $d > \xi$, followed by the linear array (at $d \sim \xi$) and parallel x-z array (at $d < \xi$). In this regime, the parallel x-y array gives the lowest value of the PMF at any given d, followed by the linear array and the parallel x-z array. The parallel x-y array is the most stable configuration in this case. The Landau–de Gennes (LdG) contribution to the PMF [Fig. 4(b)] for each array is close to zero at large particle separations, but as d is reduced the LdG PMF starts to increase until it reaches a maximum. The value of d at which the maximum is reached is larger for the parallel x-y array, followed by the linear and parallel x-z arrays; moreover, the value of the LdG PMF maximum is comparable for both parallel arrays ($\sim 13\ k_B T$), and smaller for the linear array ($\sim 5\ k_B T$). As d is reduced further, the LdG PMF curves start to decrease and eventually become negative. In contrast to the LdG PMF, the elastic contribution to the PMF [Fig. 4(c)] for each array follows the same trends previously described for the total PMF curves. In analogy to the uniparticle system, the free energy differences observed at the minima in the elastic PMF are larger in magnitude than those seen at the maxima of the LdG PMF (e.g., $\sim 70\ k_B T$ and $\sim 12\ k_B T$, respectively, for the parallel x-y array). However, these free energy differences are similar in the parallel x-z array. The maximum interparticle attractive energy is on the order of 80 $k_B T$ and 35 $k_B T$ for the parallel x-y and linear arrays, respectively, and on the order of only a few $k_B T$ for the parallel x-z array.

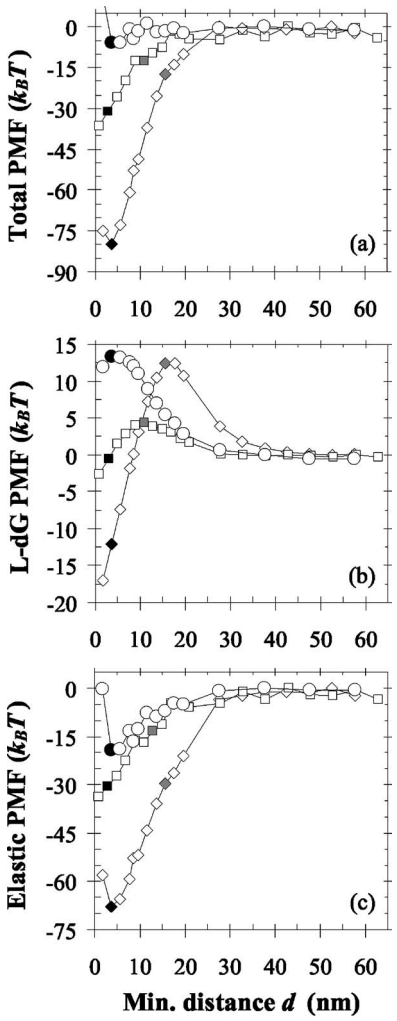

FIG. 4. Potential of mean force (PMF) for two spherocylindrical nanoparticles immersed in a nematic liquid crystal, as a function of the minimum surface-to-surface interparticle distance d. (a) Total PMF; (b) Landau–de Gennes contribution; and (c) elastic contribution. Squares: linear array, diamonds: parallel x-y array, circles: parallel x-z array. Visualizations of the configurations corresponding to the points colored in grey and black are presented in Figs. 5 and 6, respectively.

In Fig. 5 we present visualizations of the defect structures obtained at the maxima of the LdG PMF (the points colored in gray in Fig. 4). In Fig. 6 we show the defect structures obtained close to the minima of the elastic PMF (the points colored in black in Fig. 4). For all arrays, each spherocylinder is surrounded by a Saturn ring defect structure when the nanoparticles are far apart [Fig. 2(a)]. For the linear and parallel x-y arrays, at a given interparticle separation d the defect structures around the nanoparticles start to interact. As d is reduced, the Saturn rings around each spherocylinder extend toward each other in the interparticle region, becoming more and more distorted and finally fusing together [Figs.

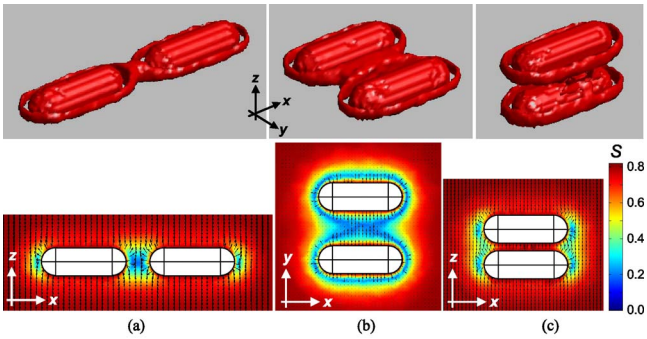

FIG. 5. (Color online) 3D visualizations of the defect structures (represented as the contour $S=0.25$, top), and contour maps of the scalar order parameter S superimposed with the director field in different planes (bottom), for two elongated nanoparticles in (a) linear array, $d=10.9$ nm, (b) parallel x-y array, $d=15.6$ nm, and (c) parallel x-z array, $d=3.6$ nm. These visualizations correspond to the maxima in the Landau–de Gennes contribution to the PMF (the points colored in grey in Fig. 4).

5(a) and 5(b)]. Upon further reduction in d, we observe a defect structure consisting of two incomplete Saturn rings, connected to a third disclination ring in the space between the nanoparticles; the latter ring is orthogonal to the original ones [Figs. 6(a) and 6(b)]. An equivalent disclination structure was observed in studies of two spherical nanoparticles [23,24]. As discussed there, this defect structure forms when the particles are close to each other because the local homeotropic anchoring can persist in the interparticle space, and therefore a "bridge" of director lines forms. These are observed in the S contour and director field maps of Figs. 6(a) and 6(b), and they are represented by the third ring "holes" in the corresponding 3D visualizations of the defect structures. Microscopically, this would correspond to a few layers of liquid crystal molecules connecting the nanoparticles. Outside this interparticle "bridge" region, the local homeotropic anchoring of the surfaces is in conflict with the bulk director field, and this produces the formation of the third disclination ring and the two Saturn rings around each particle [23,24]. For the case of two particles in a parallel x-z array, there is no formation of a third disclination ring; the Saturn rings around each nanoparticle persist disconnected down to very small values of the minimum interparticle distance d, when they start to fuse together [Figs. 5(c) and 6(c)].

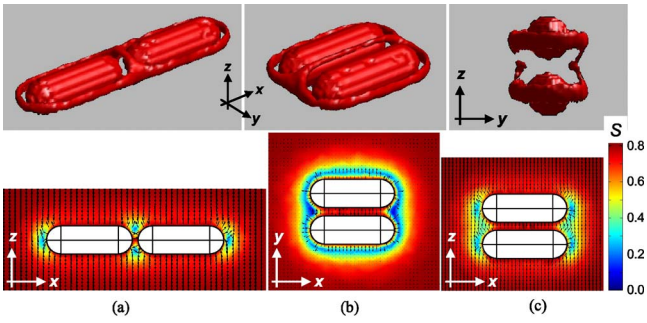

FIG. 6. (Color online) 3D visualizations of the defect structures (represented as the contour $S=0.25$, top), and contour maps of the scalar order parameter S superimposed with the director field in different planes (bottom), for two elongated nanoparticles in (a) linear array, $d=2.9$ nm, (b) parallel x-y array, $d=3.6$ nm, and (c) parallel x-z array, $d=3.6$ nm. These visualizations correspond to points close to the minima in the elastic contribution to the PMF (the points colored in black in Fig. 4). The visualizations for the parallel x-z array are equivalent to those presented in Fig. 5(c), since for this array the minimum and the maximum in the elastic and Landau–de Gennes contributions to the PMF occur at the same distance d.

Now we can analyze the PMF curves presented in Fig. 4, with the help of the defect structures shown in Figs. 5 and 6. First, the maximum in each of the LdG PMF curves [Fig. 4(b)] takes place in configurations where the Saturn rings become very distorted, i.e., when they extend toward each other and fuse together. At these points, the size of the defect structure (and therefore the amount of nematic that "melts" in the defect core) reaches a maximum. The defect structure is smaller for the linear array than for the parallel arrays (Fig. 5), which explains why the maximum in the LdG PMF for the former configuration is smaller than those for the latter arrays. In contrast, the defect structures for both parallel arrays have similar sizes (Fig. 5), and this might be responsible for the similar LdG PMF maximum values that arise for both arrays [Fig. 4(b)]. For the linear and parallel x-y arrangements, further reductions in d produce defect structures with smaller areas [e.g., compare Figs. 5(b) and 6(b)] and the LdG PMF decreases. On the other hand, the visualizations of Fig. 6 correspond to configurations close to the minimum of the elastic PMF [Fig. 4(c)]; these configurations are also close to the minima in the total PMF [Fig. 4(a)]. In these systems, the liquid crystal in the interparticle region becomes highly ordered, with $S=S_{bulk}$, and also distortions in the director field are minimized. The interparticle region is larger for the parallel x-y and x-z arrays, as compared to that of the linear array. Curvature effects are also present: in a linear array, the liquid crystal in the interparticle region experiences a larger curvature effect (from the spherical tips of both nanoparticles), as compared to the interparticle fluid in a parallel x-y or x-z arrangements (from the cylindrical sections of both particles); splay effects are therefore more important in a linear array. Another factor to consider is that both parallel x-y and linear arrays form defect structures with a third disclination ring, as opposed to the parallel x-z array, which does not. Our results suggest that the combination of these three factors influences the relative stability of the different arrays. Even though the interparticle region has the same size in both parallel configurations, the parallel x-z array does not exhibit the formation of orthogonal rings; furthermore, and in contrast to the other arrays, the minimum and maximum in the elastic and LdG PMF occur at the same distance d, and their magnitudes are similar. The minimum in the total PMF for this configuration is therefore on the order of only a few k_BT. Among the linear and parallel x-y arrays, the orthogonal disclination ring and the interparticle region are smaller for the former configuration, for which curvature effects in this "bridging" region are more important. As a result, the interparticle interaction energies are lower, $\sim 35\ k_BT$ in the linear array, as compared to $80\ k_BT$ in the parallel x-y array.

2. Three-elastic-constant expression of Edwards et al. [38–40]

In order to determine the possible effect of splay and bend distortions in our systems, we have repeated our calculations

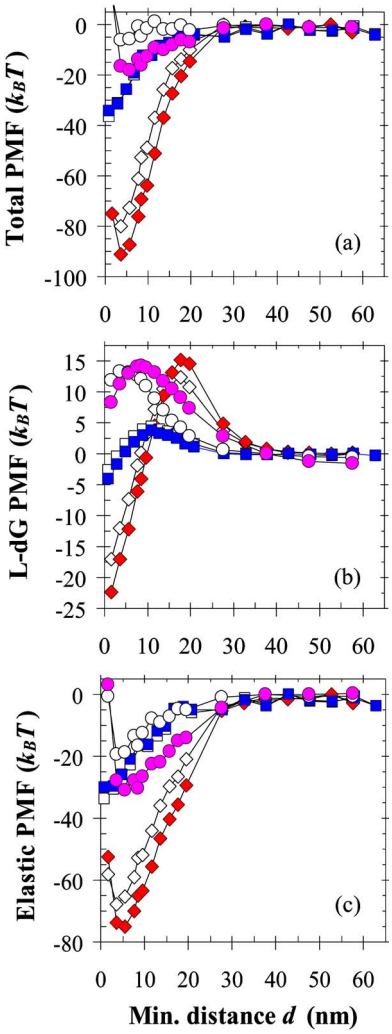

FIG. 7. (Color online) Potential of mean force (PMF) for two spherocylindrical nanoparticles immersed in a nematic liquid crystal, as a function of the minimum surface-to-surface interparticle distance d. (a) Total PMF; (b) Landau–de Gennes contribution; and (c) elastic contribution. Diamonds, squares, and circles represent values for the parallel x-y, linear, and parallel x-z arrays, respectively. Open symbols: one-elastic-constant approximation; filled symbols: three-elastic-constant expression of Edwards *et al.* [38–40].

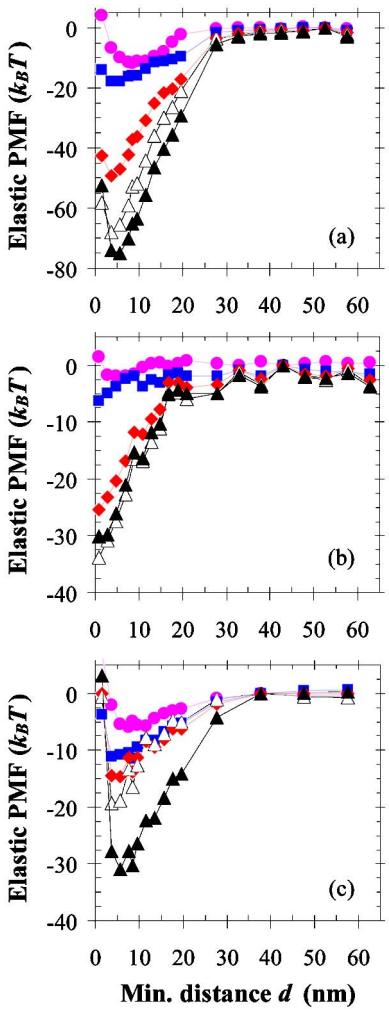

FIG. 8. (Color online) Elastic part of the potential of mean force (PMF) for two spherocylindrical nanoparticles immersed in a nematic liquid crystal, as a function of the minimum surface-to-surface interparticle distance d. (a) Parallel x-y array; (b) linear array; and (c) parallel x-z array. White triangles: one-elastic-constant approximation; black triangles: total elastic PMF from the three-elastic-constant expression of Edwards *et al.* [38–40]. Diamonds, squares, and circles represent the partial contributions from the L_1, L_2, and L_3 terms.

for the different two-particle configurations using a three-constant description for the elastic free energy [Eqs. 7–11]. In Fig. 7 we compare results for the potential of mean force for the different two-particle arrays, obtained using the three- and one-elastic constant equations. Both series of results follow the same trends: the most stable configuration is the parallel x-y array, followed by the linear and the parallel x-z array. When the three-elastic-constant description [Eq. (7)] is used, the maximum interparticle energy for the parallel arrays becomes about 10 k_BT more attractive, as compared to when the one-elastic-constant description is used (a change of 14% for the parallel x-y array). These changes come mainly from a reduction in the minima of the elastic contribution to the PMF [Fig. 7(c)]. In addition, for both parallel arrays the maxima in the LdG contribution to the PMF increases a few k_BT, and is displaced to slightly larger values of d [Fig. 7(b)], as compared to our previous results from the one-elastic-constant approximation. In contrast, the PMF curves for the linear array seems to be unaffected by using three- or one-elastic-constant expressions for the elastic free energy. We have also determined the partial contributions of the L_1, L_2, and L_3 terms to the total elastic PMF for all the two-particle arrays (Fig. 8), from which it is apparent that the main contribution comes from the L_1 term, followed by the L_2 and L_3 terms. It is worth mentioning that the L_1 term is the same in the three- or one-elastic-constant expressions [Eqs. (7) and (5), respectively]. We have also obtained the defect structures that arise when the elastic free energy is represented by the three-elastic-constant expression. We have found that these defect structures are very similar to those obtained from the one-elastic-constant ap-

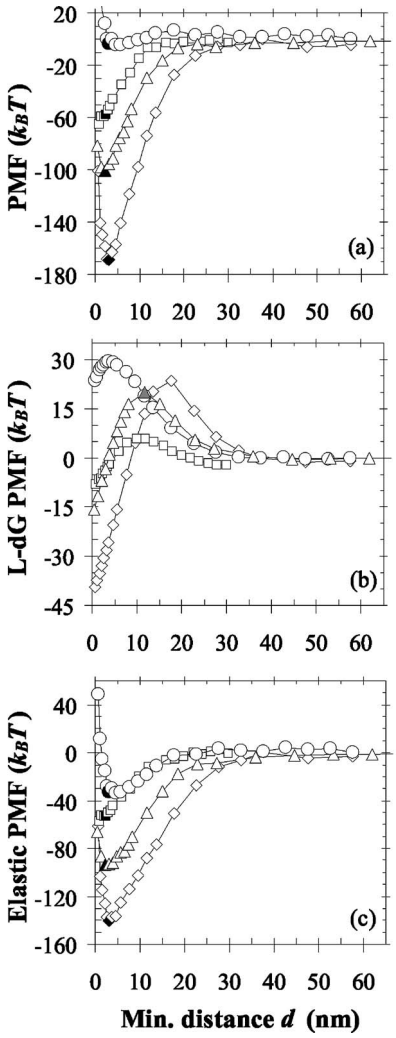

FIG. 9. Potential of mean force (PMF) for three spherocylindrical nanoparticles immersed in a nematic liquid crystal, as a function of the minimum surface-to-surface interparticle distance d. (a) Total PMF; (b) Landau–de Gennes contribution; and (c) elastic contribution. Squares, linear array; diamond, parallel x-y array; circles, parallel x-z array; triangles, triangular array. Visualizations of the configurations corresponding to the points colored in grey and black are presented in Figs. 10 and 11, respectively.

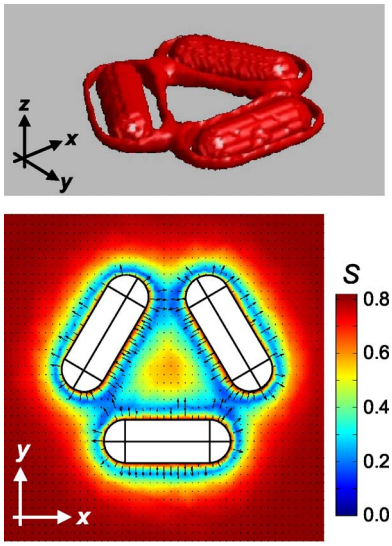

FIG. 10. (Color online) 3D visualization of the defect structure (represented as the contour $S=0.25$, top), and contour map of the scalar order parameter S superimposed with the director field in the x-y plane (bottom), for three elongated nanoparticles in a triangular array, $d=11.6$ nm. These visualizations correspond to the maxima in the Landau–de Gennes contribution to the PMF (the point colored in grey in Fig. 7).

proximation (Figs. 5 and 6). These results strongly suggest that removing the degeneracy $K_{11}=K_{33}$, and therefore distinguishing between splay and bend elastic constants, does not affect the main conclusions outlined in the previous section for the two-particle systems, within the framework of the one-elastic-constant approximation. These results also suggest that such an approximation is sufficient to capture the essential physics of the problem. We expect that removing the degeneracy $K_{11}=K_{33}$ will be very important for spherocylindrical particles of larger aspect ratio L/σ (in our case, $L/\sigma=3$), and possibly for systems of μm-sized spherocylindrical particles. These studies, however, are beyond the scope of the current manuscript.

It is of interest to compare our PMF results for elongated nanoparticles with those obtained for two spherical particles of comparable diameter [24]. Using the simulation parameters from that study to map the energy scales, we obtain an estimate of $\sim 40\ k_BT$ for the maximum interparticle interaction when an orthogonal disclination ring is observed. This energy is comparable to the value obtained for spherocylinders in a linear array ($35\ k_BT$). This is expected since the particles have similar diameters, and thus the size of both the orthogonal disclination ring and the interparticle region, and the curvature effects in such a region, are similar in both cases. However, the interparticle energy for the spherical case is lower than that corresponding to spherocylinders in a parallel x-y array, for which an energy of $80\ k_BT$ was obtained. These results can be explained by considering that the spherocylinders' total length is 2.5 times the sphere diameter. Therefore, in a parallel x-y array of spherocylinders, the size of both the orthogonal disclination ring and the interparticle region are larger, and the curvature effects in such region are smaller than those corresponding to an array of two spheres.

We can also elaborate on the possible effects of varying the spherocylinder dimensions, by comparing the results of Figs. 4 and 5 with those obtained in previous studies for two spherical particles [23,24]. On the one hand, the free energy difference between the linear and parallel x-y arrays for two elongated nanoparticles is expected to decrease as the sphere limit is approached (where both arrays would be equivalent), namely by reducing the spherocylinder total length $L+\sigma$, or by increasing the spherocylinder diameter σ. On the other hand, we anticipate that increasing the total length or decreasing the diameter will yield larger differences in free energy between the linear and parallel x-y arrays. We expect

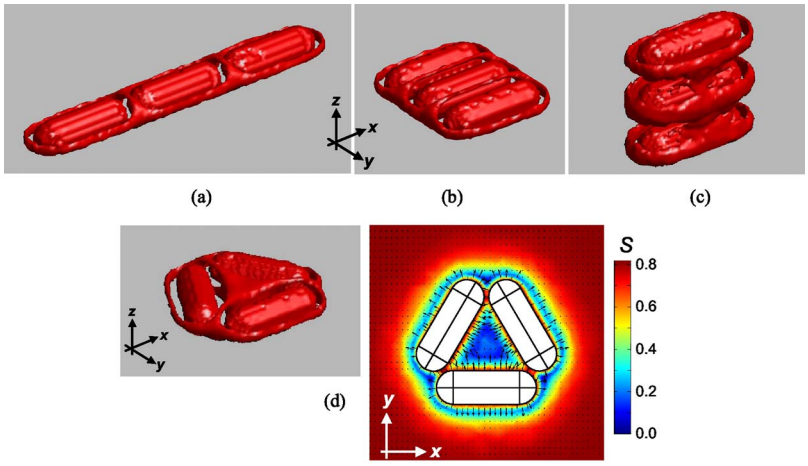

FIG. 11. (Color online) 3D visualizations of the defect structures (represented as the contour $S=0.25$), for three elongated nanoparticles in (a) linear array, $d=2.4$ nm, (b) parallel x-y array, $d=3.1$ nm, (c) parallel x-z array, $d=3.1$ nm, and (d) triangular array, $d=2.1$ nm. A contour map of the scalar order parameter S superimposed with the director field in the x-y plane is also included for the triangular array. These visualizations corresponds to points close to the minima in the PMF curves (the points colored in black in Fig. 9).

that the results for the parallel x-z array would remain unperturbed upon variations of the particle dimensions.

C. Three-particle systems

Four cases were considered for three-particle systems: (a) a linear array, (b) a parallel array in the x-y plane, (c) a parallel array in the x-z plane, and (d) a triangular array. The director field **n** is parallel to the z axis far away from the spherocylinders, as in the two-particle systems, and the one-elastic-constant approximation was used. As before, the defect structures and the potential of mean force were determined as a function of the minimum surface-to-surface interparticle distance d. Results for the potential of mean force are presented in Fig. 9. In analogy to the two-particle systems, all the total PMF curves [Fig. 9(a)] become negative as the interparticle separation d is reduced. The parallel x-y array is again the most stable configuration, followed by the triangular, linear and parallel x-z arrays. Both the Landau–de Gennes (LdG) and elastic contributions to the PMF [Figs. 9(b) and 9(c), respectively] follow the same trends described before for the two-particle systems. The curves for the LdG PMF exhibit maxima at distinct values of d in each array, and these maxima are on the order of 6, 19, 24, and 30 k_BT for the linear, triangular, parallel x-y, and parallel x-z arrays, respectively. On the other hand, the elastic contributions to the PMF show minima also at different values of d for each array, and these minima are larger in magnitude (33, 53, 94, and 141 k_BT for the parallel x-z, linear, triangular, and parallel x-y arrays, respectively) as compared to the maxima in the LdG PMF. The maximum interparticle attractive energy is on the order of 170, 100, 60, and 4 k_BT for the parallel x-y, triangular, linear, and parallel x-z arrays, respectively.

In Fig. 10 we present visualizations of the defect structure obtained at the maximum of the LdG PMF for the triangular array (the point colored in gray in Fig. 9; the corresponding defect structures for the other arrays are similar to those observed for two-particle systems). In addition, in Fig. 11 we show the defect structures obtained close to the minima of the elastic PMF for all arrays (the points colored in black in Fig. 9). In close analogy to their two-particle counterparts, for the linear and parallel x-y arrays we can observe the same sequence of defect structures as the nanoparticles are brought together. First we observe distinct Saturn rings, followed by distorted cores, and then formation of additional rings orthogonal to the original ones [Figs. 11(a) and 11(b)]. The same sequence of defect structures is observed for the triangular array. The original Saturn rings fuse together at the triangle vertices (Fig. 10), and upon further reduction of d, the central triangular interparticle region fills with a melted nematic [Fig. 11(d)]. Finally, for the parallel x-z array we do not observe the formation of additional orthogonal disclination rings; at small separations, the original Saturn rings start to fuse together [Fig. 11(c)], again in analogy to the two-particle system.

The PMF results of Fig. 9 and thus the relative stability of the different arrays can be analyzed again by considering some of the factors discussed above in the context of two particles, namely whether orthogonal disclination rings are present or not, their relative size, and the size and curvature effects in the interparticle region. The parallel x-z array does not form orthogonal rings; the minimum and maximum in the elastic and LdG PMF take place at the same distance d, and their magnitudes are similar. As before, the minimum in the total PMF for this configuration is on the order of a few k_BT. In contrast, two and three small orthogonal disclination rings, and two large rings appear in the linear, triangular, and parallel x-y arrays, respectively. Among these configurations, the curvature effects in the interparticle "bridging" regions are more important in the linear and triangular arrays, as compared to the parallel x-y configuration. As a result, the interparticle interaction energies are considerably large in these three cases, and increase from ~ 60 k_BT in the linear array, to ~ 100 k_BT in a triangular configuration, and to ~ 170 k_BT in a parallel x-y array.

We have done similar calculations for the three-particle systems using the three-elastic-constant expression [Eqs. (7)–(11)]. For the linear and parallel arrays, the main effects in the PMF and defect structures are very similar to those observed in their two-particle counterparts. For the triangular array, the effects are intermediate between those observed for the linear and parallel arrays, i.e., a very slight reduction in the total and elastic PMF. Therefore, the one-elastic-constant approximation is again sufficient to capture the essential physics of the three-particle systems.

Guzmán *et al.* [25] found that a triangular array of spherical nanoparticles immersed in a nematic liquid crystal was more stable than a three-particle linear array. Based on their simulation parameters, we obtain an estimate of 72 and 50 k_BT for the sphere interparticle interaction energy in triangular and linear arrays. These quantities are to be compared against energy values of 170, 100, and 60 k_BT, for parallel x-y, triangular, and linear arrays of three spherocylinders. As in the two-particle case, the energies for the linear arrays are similar, because the particles have similar diameters and thus the size of both the orthogonal disclination rings and the interparticle regions, and the curvature effects in such regions, are very similar. Those effects are different when comparing the other cases, since the spherocylinders total length is about 2.5 times the sphere diameter. Therefore, the orthogonal disclination rings and the interparticle regions are larger, and the curvature effects in such regions are smaller when comparing both triangular arrays, and when the parallel x-y configuration of spherocylinders is compared with the spheres' arrays.

Based on the results presented here and those published earlier for spherical particles [25], we can further elaborate on the possible effects of changes in the spherocylinder dimensions. We expect the difference in interparticle energy between the different arrays to become larger as we increase the spherocylinders length or decrease their diameter. On the other hand, as we approach the spherical particle limit (i.e., by reducing the spherocylinders length or increasing their diameter), we expect that the difference in PMF between the parallel x-y and the linear arrays will decrease, until they finally become equivalent in the spherical limit. Even though we anticipate that the PMF curve for the triangular array will also move to higher values as the spherical limit is approached, we expect that at some point the triangular array will become the most stable configuration, as was observed for the spherical case [25].

IV. CONCLUDING REMARKS

Using a dynamic field theory for the tensor order parameter **Q** and a finite element method, we have determined the defect structures and potential of mean force that arise when spherocylindrical nanoparticles are immersed in a nematic liquid crystal. Different configurations with one, two, and three elongated nanoparticles with strong homeotropic anchoring were analyzed, within the framework of the one-elastic-constant approximation. For systems containing one nanoparticle, the most stable configuration is achieved when the spherocylinder is placed with its long axis perpendicular to the far-field director, for which the defect structure consists of a Saturn ring around the equatorial plane of such axis. As the angle between the long axis of the particle and the far-field director is reduced, the disclination ring becomes distorted and its width increases, until it eventually surrounds the cylindrical section of a particle that is parallel to the far-field director. These results for an isolated nanoparticle are in good agreement with those of molecular simulations [31].

For systems of two or three elongated nanoparticles having their long axes perpendicular to the director field, at small separations the defect structures consist of incomplete Saturn rings fused with new disclination rings that are orthogonal to the original ones. These structures are similar to those previously reported in systems of spherical nanoparticles immersed in liquid crystal [23–25], and give rise to an important effective attraction between the nanoparticles. The formation of these extra-ring disclination structures depends on the way the elongated particles are brought together. If the director field is parallel to the z axis, these defect structures are observed in linear, parallel x-y, and triangular arrays; in all these cases, the particles' long axes are always perpendicular to the director field. Such defect structures with additional rings were not observed when the particles were arranged in a parallel x-z array. Results for the potential of mean force indicate that in all cases, the most stable structure is the parallel x-y array. These results can be fully rationalized by considering whether orthogonal disclination rings are present or not, their relative size, and the size and curvature effects in the interparticle regions.

In order to determine the possible effect of splay and bend distortions in our systems, we have repeated our calculations for the two- and three-particle systems using the elastic free energy form proposed by Edwards *et al.* [38–40], which includes three elastic coefficients and cubic terms in **Q** and its gradients [Eqs. (7)–(11)]. This expression for the elastic free energy removes the degeneracy $K_{11}=K_{33}$ that is implicit in the one-elastic-constant approximation. The potential of mean force and the defect structures obtained using this three-elastic-constant description were very similar to their one-elastic-constant counterparts, thereby suggesting that the latter approach is sufficient to capture the essential physics of our systems.

The effective, liquid crystal-induced attractive interactions between elongated particles were also compared to those observed for nm-sized spheres of similar diameters. Similar interparticle energies were observed for linear arrays; in contrast, parallel and triangular arrays of spherocylinders yielded interparticle interactions that were up to 3.4 times larger than those observed in similar arrays of spherical nanoparticles. Large liquid crystal-induced effective attractions between elongated nanoparticles could have implications in a number of emerging applications. As an example, new composite materials could be developed where the nematic director field points along the z axis, while the elongated nanoparticles self-assemble with their long axes parallel to each other and pointing along the x axis. Note that the results presented in this work correspond to elongated, nanoscopic-size particles immersed in a nematic liquid crystal. Equivalent efforts for μm-sized anisotropic particles are currently under way. Our future work will also focus on studying the structure and dynamics of 3D nematic films confined between parallel walls in the presence of adsorbed nanoparticles. We are also interested in systems where freely moving particles are dispersed into a flowing liquid crystal. These systems are relevant for practical applications in colloidal dispersions and liquid crystal sensors, among others.

ACKNOWLEDGMENTS

We are grateful to P. Poulin for suggesting the calculations described in this work and for very helpful discussions. F. R. H. also thanks E. Santiso for enlightening discussions. This work was supported by the University of Wisconsin Nanoscale Science and Engineering Center (NSEC) on Templated Synthesis and Assembly at the Nanoscale (Research Thrust 3, Driven Nano-Fluidic Self-Assembly of Colloids and Macromolecules).

[1] V. K. Gupta, J. J. Skaife, T. B. Dubrovsky, and N. L. Abbott, Science **279**, 2077 (1998).
[2] R. R. Shah and N. L. Abbott, Science **293**, 1296 (2001).
[3] J. M. Brake, M. K. Daschner, Y. Y. Luk, and N. L. Abbott, Science **302**, 2094 (2003).
[4] P. Poulin, H. Stark, T. C. Lubensky, and D. A. Weitz, Science **275**, 1770 (1997).
[5] P. Poulin, Curr. Opin. Colloid Interface Sci. **4**, 66 (1999).
[6] J. C. Loudet, P. Barois, and P. Poulin, Nature (London) **407**, 611 (2000).
[7] S. P. Meeker, W. C. K. Poon, J. Crain, and E. M. Terentjev, Phys. Rev. E **61**, R6083 (2000).
[8] J. C. Loudet, P. Barois, P. Auroy, P. Keller, H. Richard, and P. Poulin, Langmuir **20**, 11336 (2004).
[9] P. G. de Gennes and J. Prost, *The Physics of Liquid Crystals* (Clarendon, Oxford, 1993).
[10] N. Schopohl and T. J. Sluckin, Phys. Rev. Lett. **59**, 2582 (1987).
[11] P. Poulin and D. A. Weitz, Phys. Rev. E **57**, 626 (1998).
[12] O. Mondain-Monval, J. C. Dedieu, T. Gulik-Krzywicki, and P. Poulin, Eur. Phys. J. B **12**, 167 (1999).
[13] Y. Gu and N. L. Abbott, Phys. Rev. Lett. **85**, 4719 (2000).
[14] R. W. Ruhwandl and E. M. Terentjev, Phys. Rev. E **55**, 2958 (1997).
[15] R. W. Ruhwandl and E. M. Terentjev, Phys. Rev. E **56**, 5561 (1997).
[16] T. C. Lubensky, D. Pettey, N. Currier, and H. Stark, Phys. Rev. E **57**, 610 (1998).
[17] H. Stark, Eur. Phys. J. B **10**, 311 (1999).
[18] H. Stark, Phys. Rep. **351**, 387 (2000).
[19] S. Grollau, N. L. Abbott, and J. J. de Pablo, Phys. Rev. E **67**, 011702 (2003).
[20] J. Fukuda, M. Yoneya, and H. Yokoyama, Eur. Phys. J. E **13**, 87 (2004).
[21] J. Fukuda, H. Stark, M. Yoneya, and H. Yokoyama, Phys. Rev. E **69**, 041706 (2004).
[22] J. Fukuda and H. Yokoyama, Phys. Rev. Lett. **94**, 148301 (2005).
[23] O. Guzmán, E. B. Kim, S. Grollau, N. L. Abbott, and J. J. de Pablo, Phys. Rev. Lett. **91**, 235507 (2003).
[24] E. B. Kim, O. Guzmán, S. Grollau, N. L. Abbott, and J. J. de Pablo, J. Chem. Phys. **121**, 1949 (2004).
[25] O. Guzmán, N. L. Abbott, and J. J. de Pablo, J. Polym. Sci., Part B: Polym. Phys. **43**, 1033 (2005).
[26] S. Grollau, O. Guzmán, N. L. Abbott, and J. J. de Pablo, J. Chem. Phys. **122**, 184711 (2005).
[27] O. Guzmán, N. L. Abbott, and J. J. de Pablo, J. Chem. Phys. **122**, 024703 (2005).
[28] C. Lapointe, A. Hultgren, D. M. Silevitch, E. J. Felton, D. H. Reich, and R. L. Leheny, Science **303**, 652 (2004).
[29] C. Lapointe, N. Cappallo, D. H. Reich, and R. L. Leheny, J. Appl. Phys. **97**, 10Q304 (2005).
[30] S. V. Burylov and Y. L. Raikher, Phys. Rev. E **50**, 358 (1994).
[31] D. Andrienko, M. P. Allen, G. Skačej, and S. Žumer, Phys. Rev. E **65**, 041702 (2002).
[32] D. Andrienko, M. Tasinkevych, P. Patrício, M. P. Allen, and M. M. Telo da Gama, Phys. Rev. E **68**, 051702 (2003).
[33] D. Andrienko, M. Tasinkevych, P. Patrício, and M. M. Telo da Gama, Phys. Rev. E **69**, 021706 (2004).
[34] D. Andrienko, M. Tasinkevych, and S. Dietrich, Europhys. Lett. **70**, 95 (2005).
[35] G. McKay and E. G. Virga, Phys. Rev. E **71**, 041702 (2005).
[36] R. Yamamoto, Phys. Rev. Lett. **87**, 075502 (2001).
[37] R. Yamamoto, Y. Nakayama, and K. Kim, J. Phys.: Condens. Matter **16**, S1945 (2004).
[38] A. N. Beris and B. J. Edwards, *Thermodynamics of Flowing Systems with Internal Microstructure* (Oxford University Press, New York, 1994).
[39] B. J. Edwards and A. N. Beris, J. Rheol. **33**, 1189 (1989).
[40] B. J. Edwards, A. N. Beris, and M. Grmela, J. Non-Newtonian Fluid Mech. **35**, 51 (1990).
[41] L. Longa, D. Monselesan, and H.-R. Trebin, Liq. Cryst. **2**, 769 (1987).
[42] M. C. J. M. Vissenberg, S. Stallinga, and G. Vertogen, Phys. Rev. E **55**, 4367 (1997).
[43] G. Marrucci and F. Greco, Mol. Cryst. Liq. Cryst. **206**, 17 (1991).
[44] M. Cui and J. R. Kelly, Mol. Cryst. Liq. Cryst. Sci. Technol., Sect. A **331**, 49 (1999).
[45] *COMSOL Multiphysics™ Version 3.2 User's Guide* (COMSOL, Inc., Burlington, MA, 2005), and references therein. http://www.comsol.com/
[46] For the case of Eq. (6), the elastic term $L_1\partial_k\partial_k Q_{ij}$ and the Landau–de Gennes terms were included as part of the diffusive flux (c) and source (f) terms, respectively, of the coefficient PDE form of COMSOL Multiphysics™. For Eq. (11), again the expressions arising from the Landau–de Gennes part were introduced in the source term f. In the elastic part, the terms associated with second spatial derivatives of **Q** were included in the diffusive flux term c, and those linked to first spatial derivatives of **Q** were introduced as part of the convection term β. The models were created, executed, and saved as a MATLAB® M file.
[47] S. Kralj, E. G. Virga, and S. Žumer, Phys. Rev. E **60**, 1858 (1999).
[48] S. Kralj and E. G. Virga, J. Phys. A **34**, 829 (2001).
[49] S. Kralj and E. G. Virga, Phys. Rev. E **67**, 021703 (2002).